ELSEVIER

Journal of Fluids and Structures 23 (2007) 531–544

JOURNAL OF FLUIDS AND STRUCTURES

www.elsevier.com/locate/jfs

Quantitative evaluation of flow-induced structural vibration and noise in turbomachinery by full-scale weakly coupled simulation

Y.Y. Jiang*, S. Yoshimura, R. Imai, H. Katsura, T. Yoshida, C. Kato

FSIS, Institute of Industrial Science, The University of Tokyo, 4-6-1 Komaba, Meguro-ku, Tokyo 153-8505, Japan

Received 3 November 2005; accepted 13 October 2006
Available online 8 December 2006

Abstract

This article reports on a full-scale structural simulation of flow-induced mechanical vibrations and noise in a 5-stage centrifugal pump. An interior flow field is simulated by an LES-based CFD program, which can be found elsewhere. We developed a data-interface tool to enable mesh matching and data transfer between the fluid and structure meshes. The vibration of the pump's structure was simulated using a parallel explicit dynamic FEM code. This provided a time series of pressure fluctuations on the internal surface as force-boundary conditions. The calculated vibration of the outer surface of the structure agrees reasonably well with measured data. Using Fourier transformation, the vibration modes at blade passing frequencies (BPFs) were extracted and presented as a visual image. The simulation clarified the mechanisms of resonant noise generation and propagation, which can then be used for noise reduction. This study shows that it is feasible to use fluid–structure weakly coupled simulations to estimate the flow-induced noise generated in turbomachinery.

Keywords: Flow-induced noise; Fluid–structure interaction; Turbomachinery; Coupled simulation

1. Introduction

Because of its environmental impact, noise generated by turbomachinery is receiving increasing research interest. This noise can be induced by internal turbulent flow and by fluid–structure interaction (FSI). For comprehensive reviews, see Guelich and Bolleter (1992) and Rzentkowski (1996). Most previous noise-analysis work has focused on theoretical formulations or experimental measurements (Mongeau et al., 1995; Chu et al., 1995; Morgenroth and Weaver, 1996; Dong et al., 1997; Rzentkowski and Zbroja, 2000). Recently, however, direct numerical simulations provide a more promising path for this study. For instance, Kato et al. (2003) simulated the noise emitted by turbulent flow through large eddy simulation (LES) and Langthjem and Olhoff (2004a,b) performed a coupled simulation of the hydroacoustic noise of a two-dimensional laboratory pump using a discrete vortex method.

These studies have dealt with hydroacoustic noise, but have not considered noise induced by structural and mechanical vibration. Since internal-flow-induced noise radiates into the air through structural vibration, high-accuracy

*Corresponding author. Tel.: +81 3 5452 6587; fax: +81 3 5452 6545.
E-mail address: jiang@fsis.iis.u-tokyo.ac.jp (Y.Y. Jiang).

0889-9746/$ - see front matter © 2006 Elsevier Ltd. All rights reserved.
doi:10.1016/j.jfluidstructs.2006.10.003

Nomenclature

A	area
b	body force
c	sound velocity
C_M	mass damping coefficient
d	diameter
D	elastic tensor
f	frequency
F	surface force
K	stiffness
M	mass
Ma	Mach number, v/c
p	pressure
Q	monopole sound source
$s(\mathbf{x}, t)$	sound source in flow
St	Strouhal number, $\mathrm{St} = f/\omega Z_i$
T	turbulence vortex tensor
t	time
u	displacement
v	velocity
V	normalized velocity, $V = v/v_{\mathrm{tip}}$
$\mathbf{x}(x, y, z)$	position vector
Z_i	number of impeller blades

Greek letters

α	angle between two vectors
δ	velocity-gradient tensor
ε	deformation tensor
ρ	density
σ	stress tensor
ω	impeller rotation speed

Subscripts

i	impeller, component of vector
j	component of vector
tip	tip of impeller blade
w	wall

estimation requires us to include these structural effects. The authors aimed to develop a numerical algorithm for the quantitative estimation of turbomachinery noise, using a fluid–structural–acoustic weakly coupled simulation (Kato et al., 2005). In the first attempt we overcame many technical difficulties in existing numerical simulations, such as finding a means of precisely calculating turbulent unsteady flow, making efficient large-scale data transfers among different meshes (fluid, structure) and dealing with the requirement for a huge amount of computational power. Our simulation object is a 5-stage centrifugal pump manufactured by Hitachi Plant Technologies. Besides clearly showing the mechanisms of noise generation, the simulation results agreed closely (quantitatively) with actual measurements taken in an experiment. This article focuses on the structural simulation and strategies for weak coupling among simulations. The anterior-fluid and posterior-acoustic simulations can be found elsewhere (Wang et al., 2004; Takano et al., 2005).

The contents are organized as follows. Section 2 provides the theoretical basis for the weak coupling numerical scheme. Section 3 presents the techniques of mesh matching and data interpolation, as well as the numerical model. The results are discussed in Section 4. Section 5 contains some concluding remarks for future research.

2. Weakly coupled simulation scheme

Fig. 1 shows a schematic representation of a multi-stage centrifugal pump, which is of the same series as the 5-stage pump. This pump, called a boiler-feeding pump (BFP), provides high-pressure water for power-plant boilers. Fig. 2 shows the occurrence and propagation routes of flow-induced vibration and noise. The vibrations originate from pressure fluctuations in the fluid. These fluctuations stimulate the vibrations of the stator blades (diffuser and return channel), which then transfer to the outer casing through the structure. Moreover, the fluctuations can be transported through the fluid to the inside faces of the inlet and outlet nozzles and pipes, causing them to vibrate.

The noise generation and propagation processes were simulated by way of one-way weak coupling. The process is as follows: (i) Use LES to solve the internal unsteady flow. This provides a time series for the pressure fluctuations at the fluid–wall interface. (ii) Simulate the structure's elastic-wave propagation, induced by the fluid surface pressure, to obtain the vibration velocities on the outer surface. (iii) Perform acoustical simulation of noise emission to the environment. In the simulations, the feedback influences of environmental noise on the structure and of structural vibration on the fluid were neglected. Although it seems certain that environmental noise has insignificant effects on structural vibration, it does seem necessary to consider the influence of structural vibration on the internal flow. The vibrations of the structure can act on the hydraulic flow through two possible approaches. The first is the movement of

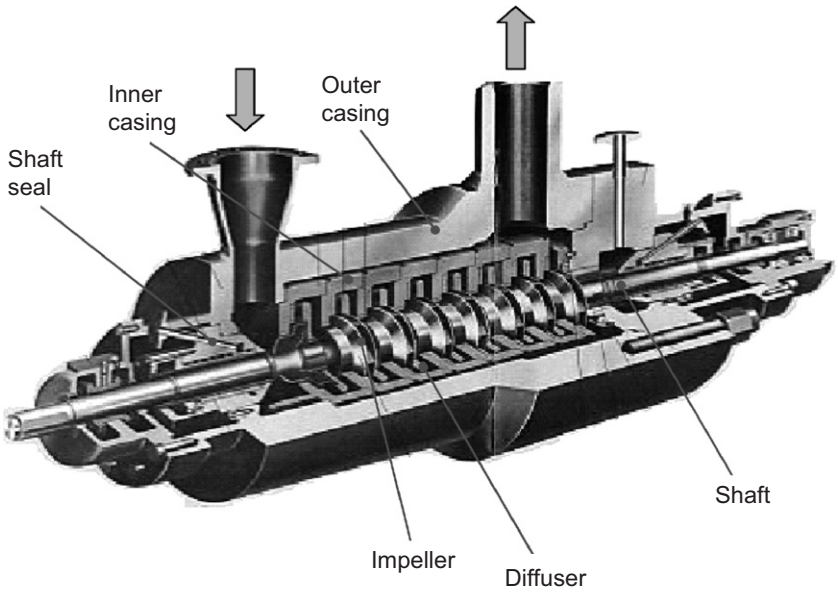

Fig. 1. Multi-stage centrifugal pump manufactured by Hitachi Plant Technologies (a model of the same series as the 5-stage pump).

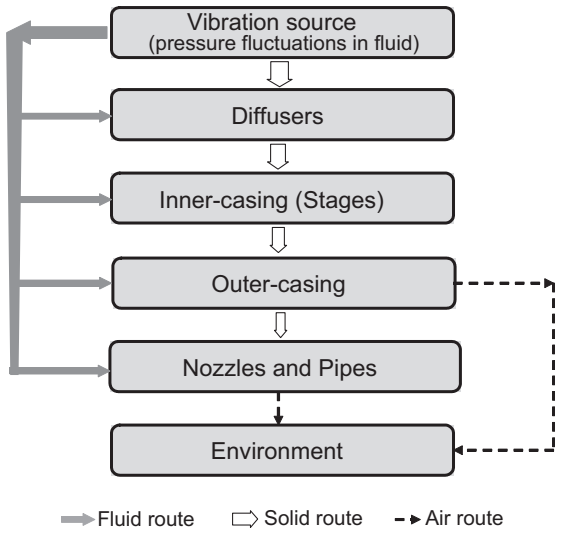

Fig. 2. Occurrence and propagation routes of centrifugal pump noise.

the fluid boundary. This effect appears insignificant, since the displacement of wall surface created by elastic vibration is usually less than 1 μm, which is much smaller than the characteristic length of the fluid flow. Thus, when simulating fluid convection in turbomachinery, a vibrating wall is seldom considered. The second means is the stimulated elastic wave, i.e. a hydroacoustic field in the fluid. In addition, the effect of hydroacoustic waves on the flow in centrifugal pumps is insignificant, because the flow is incompressible and the characteristic Mach number is much less than one (Lighthill, 1952; Howe, 1991).

The acoustic field that exists in the internal fluid can act on the structural vibration. Following the 'acoustic analogy' point of view (Lighthill, 1952), for flow characterized by a small Mach number, the sound analysis of fluid is separated into the following two steps. The first step is a hydrodynamic analysis, which is a CFD simulation to be performed to obtain 'background flow' and noise-generating fluid forces. The second step is hydroacoustic analysis, which considers the solution of an inhomogeneous wave equation. The fluid pressure fluctuations obtained at the first step are fed to the

equation as forcing functions. The generation and propagation of sound waves in a flow with a moving wall can be represented by the Ffowcs Williams and Hawkings (1969) equation

$$\nabla^2 p - \frac{1}{a^2}\frac{\partial p^2}{\partial t^2} = -s(\mathbf{x}, t), \tag{1}$$

where $p(\mathbf{x}, t)$ is a fluid pressure at position $\mathbf{x} = (x_1, x_2, x_3)$ and at time t, a is the sound speed of the fluid, and the source term $s(\mathbf{x}, t)$ is a sound-generating forcing function, written as

$$s(\mathbf{x}, t) = \frac{\partial Q}{\partial t} - \frac{\partial F_i}{\partial x_i} - \frac{\partial^2 T_{ij}}{\partial x_i \partial x_j}, \tag{2}$$

where the scalar Q, the vector F_i, and the tensor T_{ij} represent a simple force, an unsteady pressure force, and a stress distribution because of the variation of turbulent vortices, respectively, acting as monopole, dipole, and quadrupole sound sources. In a centrifugal pump, the monopole sources may exist in the form of nonuniform outflow from the impeller and of flow and stagnation pressure oscillations at the pump discharge (Langthjem and Olhoff, 2004a,b). However, these are normally weak in a well-designed pump. The quadrupole sources are found in the unsteady, highly turbulent wake flow. For a typical centrifugal pump, with 5–10 blades running at very small Mach number, the noise contribution from the quadrupoles can safely be neglected (Howe, 1991). The dipole sources exist in the form of acoustic-pressure fluctuations generated by the rotor–stator interactions. Studies have shown that these dipole sources are the dominant noise components in the internal fluid. However, the rotor–stator interactions produce simultaneously hydraulic pressure waves in the fluid as well. The hydraulic and acoustic-pressure waves have the same frequencies, while the amplitude of the latter is usually several orders smaller than that of the former. Because their frequencies are coincident, the influences of the acoustic waves on structural vibration are negligible. Therefore, we need not calculate the acoustic pressure from the dynamic flow field to take into account all the above contributions, although the CFD simulation could provide it. Instead, we input only the hydraulic pressure at the fluid–wall interface into the structural simulation.

This study is funded by a program 'Frontier Simulation Software for Industrial Science (FSIS)' supported by MECSST of Japan (http://www.fsis.iis.u-tokyo.ac.jp). Under this framework, Wang et al. (2004) performed an LES for turbulent unsteady flow, using the codename FRONTFLOW-Blue. They developed a time series for the hydraulic pressure at the fluid–wall interface. With the additional input of the fluid forces, we simulated vibration propagation in the structure, using a finite element program, named NEXST-Impact, and output the vibration velocities at the pump's outer surface. Takano et al. (2005) then used the velocity data to calculate noise emissions to the environment, using a commercial program called SYSNOISE. A data interface named MULTI-COUPLER was developed for transferring data among the three simulations. We compared the simulation results with experimental data in Katsura and Yoshida (2003).

3. Mesh matching and data transfer

3.1. Brief introduction to fluid simulation

FRONTFLOW-Blue is a general-purpose CFD program, which solves turbulent flows based on LES. The fluid mesh has 36.2 million hexahedral volume cells in total and 2.71 million surface elements at the fluid–wall boundary. The calculations were performed on a supercomputer called Earth-Simulator, using 32 nodes (160 Gflops). One impeller rotation required 12 000 calculation steps, and took 7 h. The simulation was performed for more 24 impeller rotations. Details of the computation scheme can be found in Wang et al. (2004). In the present study, our interest is the prediction of the surface pressures. In a Navier–Stokes fluid, the stress σ is a tensor, which takes the form

$$\sigma = (-p + \lambda \nabla \cdot \mathbf{v})I + 2\mu\delta, \quad \delta_{ij} = \frac{1}{2}\left(\frac{\partial v_i}{\partial x_j} + \frac{\partial v_j}{\partial x_i}\right), \tag{3}$$

where p is static pressure, μ the dynamic viscosity, λ the second viscosity, and δ_{ij} a velocity-gradient tensor. Note that at the wall boundary the velocity $\mathbf{v}$ is zero, and the shearing stress is usually much smaller than the variation of static pressure, so that Eq. (3) can be rewritten as

$$\left(\sum_j \sigma_{ij} \cdot n_i\right)\Big|_w = -p \cdot n_i, \tag{4}$$

where n_i is the surface normal vector. During the fluid simulation, the surface pressure p was output every 12 steps. Fig. 3 shows a fluctuation spectrum of the surface pressure sampled at the inlet of the second-stage diffuser. This shows that the simulation results agree with experimental data reasonably well at each blade passing frequency (BPF). BPF refers to the pressure fluctuations or structural vibrations whose frequencies are integer times of the impeller rotation speed. The BPF components dominate the vibration and noise in centrifugal pumps. Here, the unit of frequency is normalized to the Strouhal number St, which is defined as

$$\mathrm{St} = \frac{f}{\omega Z_i} = \frac{f d_i}{v_{\mathrm{tip}}} \times \frac{\pi}{Z_i}, \tag{5}$$

where d_i, ω, and Z_i are the impeller's diameter, rotation speed, and blade number, respectively, and $v_{\mathrm{tip}} = \pi d_i \omega$ denotes the impeller tip speed.

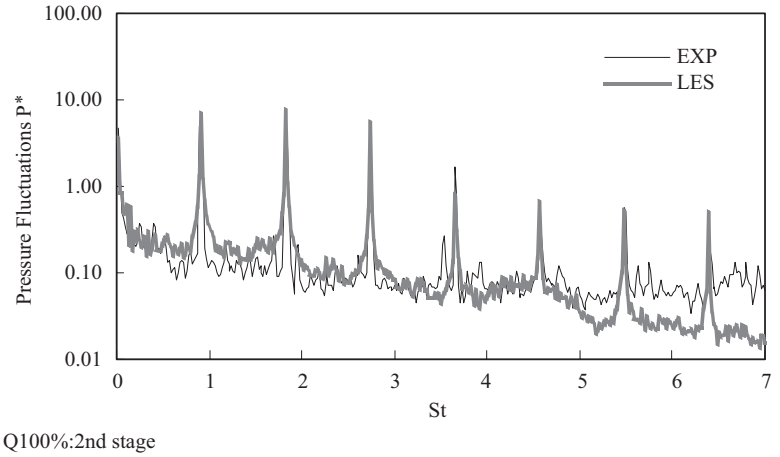

Fig. 3. Power spectrum of the fluctuation frequencies of surface pressure sampled at the inlet of the second-stage diffuser [copied with agreement from Wang et al. (2004)].

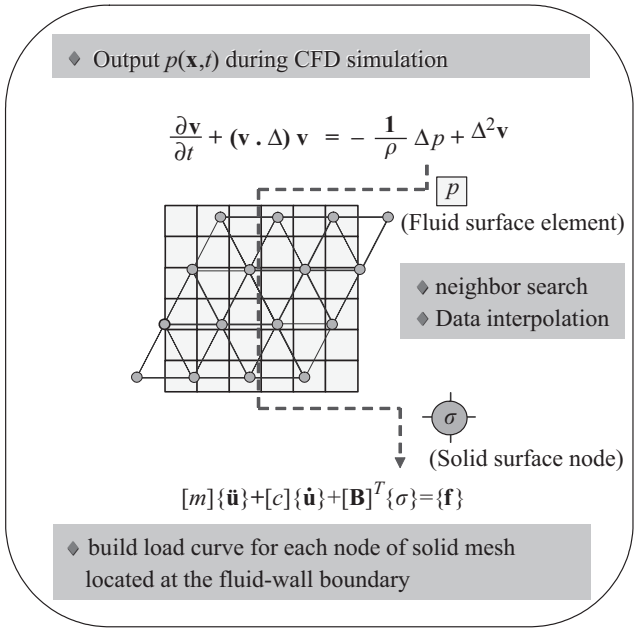

Fig. 4. Process of mesh matching and data transfer between fluid and structure meshes.

3.2. Data transfer from fluid to structure

Fig. 4 outlines the process of mesh matching and data transfer. In the CFD simulation, fluid pressures were saved in fluid surface elements (also called patches). The data were transferred, via interpolation, to surface nodes of the structural mesh. Before performing the data transfer, a structure node N_i ($i = 1, \ldots, L$) has to find its matching partner by searching for a surface element E_j ($j = 1, \ldots, M$) bound to it. To determine the matching pairs, one straightforward way is to compare all pairs of nodes and patches; however, this leads to an amount of work of $\mathcal{O}(LM)$—becoming unacceptably time consuming for large meshes. A bucket algorithm (Sekita et al., 2001) improved the search. The bucket algorithm uses a regular grid of buckets, uniform in each coordinate direction, which is superimposed on the volume region. Each cell of this grid is called a bucket, and is referred to by its bucket multi-index $B(k_1, k_2, k_3)$. One then stores each patch E_j to buckets that contain all or a part of the patch. Therefore, when searching a matching E_j for N_i, one needs only to compare the patches in the bucket box occupied by N_i.

It should be noted here that the patch should be stored in as many buckets as possible to ensure that the bucket occupied by N_i does contain the matching patch. One method is to calculate the bucket index k_i ($i = 1, 2, 3$) for every vertex of the patch to obtain an index value range $\forall\{(k_1, k_2, k_3)_E\}$ when stacking a patch. The patch will be deposited into all buckets whose index is within this range, i.e. $B(k_1, k_2, k_3) \in \forall\{(k_1, k_2, k_3)_E\}$. For a very complex mesh, the fluid surface and the structure surface may have small gaps, possibly due to the defects that occur in creating meshes. In this case, there might be a target node situated in a bucket that does not contain the potential matching patch. This problem can be avoided by enlarging the value range of $\forall(k_1, k_2, k_3)_E$ in the patch's normal directions—by moving the vertices for a specified distance in both normal directions to calculate expanded limits of the index.

Several methods could be used to determine whether a patch contains a node. One method is illustrated in Fig. 5. Suppose that the node N is usually not located in the plane of the patch E because of the surface gap. We first obtain its projecting point N' in the patch's plane. Next, for each vertex of the patch, we calculate the angle α between the vector from the vertex toward the next one, and the vector from the vertex toward N'. If $\sin\alpha$ does not change sign for all the vertices, the projecting point N' should be contained in the patch. If the distance between N and N' is less than the specified limit, patch E is judged to match the target node N. In the present study, the fluid mesh includes 2.71 million patches, and the structure mesh has 11.2 thousand nodes at the interface. It took less than 30 s to determine matching pairs with the bucket grid, while it took more than 20 h without a bucket grid.

Two data-transfer methods were used. The first, called 'forward matching' entails having a structure node look for a fluid patch that contains it. It then takes the patch's pressure p as its value. A loading boundary is then built by multiplying the pressure with the node's equivalent area, $\mathbf{F} = pA \cdot \mathbf{n}$. The second method, called 'backward matching' has every fluid patch looking for a structure patch that contains the fluid patch center. It then transfers its pressure to that structure patch, which sums all the data into a total load. The loading boundary of the structure node is then built by interpolation from structure patch to node. Because the structure mesh is 10 times coarser than the fluid mesh, the first method does not seem sufficiently precise. Most of the fluid data will not be used. However, a comparison of the results of both data-transfer methods and simulation show no significant differences. This is apparently because no sharp local variations exist in the surface pressure's spatial distribution. In Fig. 6 a distribution of the transferred pressures at a specific time are compared with the original pressures. The figure plots the excess pressures over time averages. The two distributions are in good agreement.

4. Structural simulation

4.1. Numerical model

The governing equations for dynamic elastic vibrations of structure are

$$\rho_s \frac{\partial^2 u_i}{\partial t^2} + c_s \frac{\partial u_i}{\partial t} - \frac{\partial \sigma_{ij}}{\partial x_j} - b_i = 0, \tag{6}$$

$$\sigma_{ij} = D_{ijkl}\varepsilon_{kl}, \tag{7}$$

$$\varepsilon_{ij} = \frac{1}{2}\left(\frac{\partial u_i}{\partial x_j} + \frac{\partial u_j}{\partial x_i}\right), \tag{8}$$

where u_i, D_{ijkl}, ε_{ij}, and b_i denote a displacement vector, an elastic tensor, a strain tensor, and a body force vector,

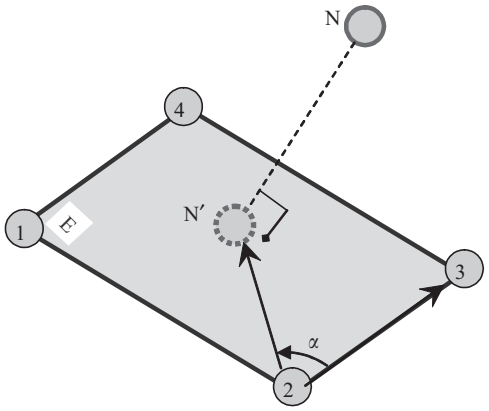

Fig. 5. Method used to determine whether a node is contained by a surface element.

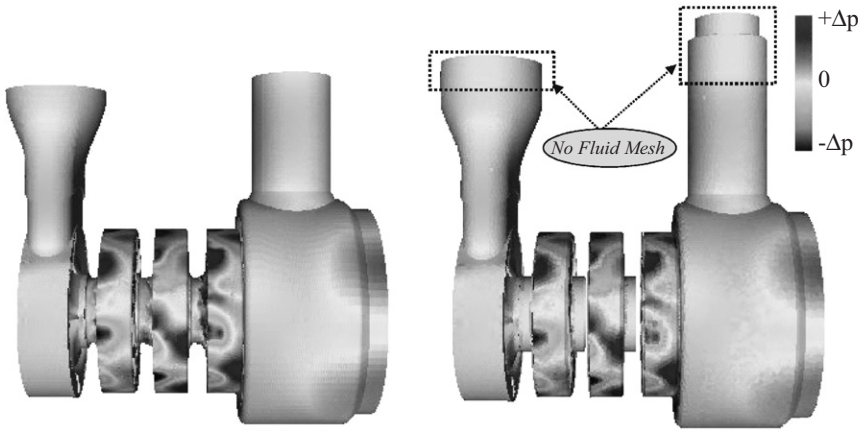

Fig. 6. Instantaneous pressure distribution at fluid–structure interface. (1) Fluid data output by CFD and (2) interpolated to structure nodes.

respectively, and c_s is a damping coefficient. The boundary conditions are

$$u_i = \bar{u}_i \quad \text{at the displacement boundary;} \tag{9}$$

$$\sum_j \sigma_{ij} n_i = p \cdot n_i \quad \text{at the force boundary.} \tag{10}$$

Eqs. (6)–(8) can be written in the matrix form

$$[\mathbf{M}]\{\ddot{\mathbf{u}}\} + [\mathbf{C}]\{\dot{\mathbf{u}}\} + [\mathbf{K}]\{\mathbf{u}\} = \{\mathbf{b}\}, \tag{11}$$

where $\{\mathbf{u}\}$ is a displacement vector, $[\mathbf{M}]$, $[\mathbf{C}]$, $[\mathbf{K}]$ are a mass matrix, a damping matrix, and a stiffness matrix, respectively. In the present calculation, the body force $\{\mathbf{b}\}$ indicates the gravity forces. The value of $[\mathbf{C}]$ is usually given by the Rayleigh's theory as

$$[\mathbf{C}] = c_K[\mathbf{K}] + c_M[\mathbf{M}]. \tag{12}$$

Here we take $c_K = 0$ and determine c_M by experimental measurements. In NEXST-Impact, the equation is discretized in a central-difference scheme, which is expressed as

$$\left\{\frac{1}{\Delta t^2}[\mathbf{M}] + \frac{1}{2\Delta t}[\mathbf{C}]\right\}\{\mathbf{u}\}_{n+1} = [\mathbf{f}]_n - \left\{[\mathbf{K}] - \frac{1}{\Delta t^2}[\mathbf{M}]\right\}\{\mathbf{u}\}_n - \left\{\frac{1}{\Delta t^2}[\mathbf{M}] - \frac{1}{2\Delta t}[\mathbf{C}]\right\}\{\mathbf{u}\}_{n-1}. \tag{13}$$

The time increment Δt obeys the Courant stability condition.

4.2. Computational conditions

The simulation was performed by NEXST-Impact, which is FEM code with parallel computation functions based on domain decomposition. Fig. 7 shows the structure mesh, which has 1.43 million 4-noded tetrahedral elements and 0.97 million degrees of freedom. The average height of the elements is 6.64 mm and minimum of 0.30 mm.The time series of the transformed fluid force was input as a loading boundary. At a time between two fluid-force steps, the load was linearly interpolated. The simulation was implemented by a supercomputer (SR8000) using 32 CPUs (running at

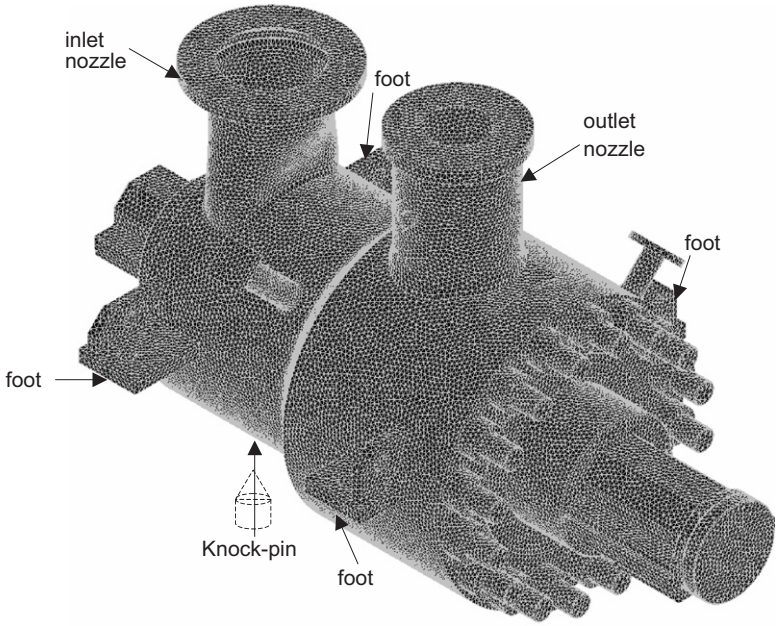

Fig. 7. Mesh used in structural simulation.

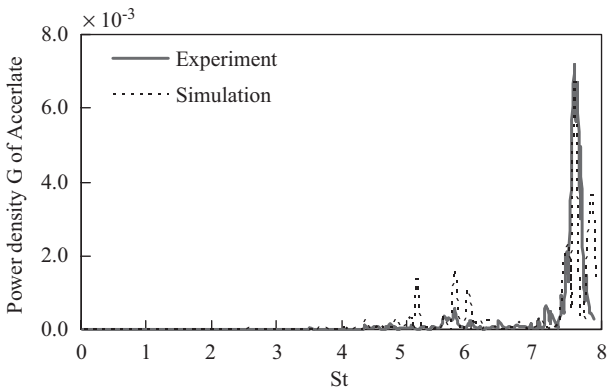

Fig. 8. Measured and calculated spectra of vibration acceleration in a hammer impact test (the knocking/measuring points are P_3/P_1).

1.34 GFlops). The simulation of one impeller rotation (184.5 thousand steps) took 1.12 h. A complete simulation consisted of 24 rotations. The first three rotations comprised of a starting stage, after which the vibration time series no longer has global fluctuations, and the results can be sampled for analysis.

In the experiment, the pump's four feet and a knock-pin at the bottom of the inlet body were fixed to a foundation. The inlet and outlet nozzles were connected to pipelines. In our simulation, the boundary conditions and the coefficient of Rayleigh dumping c_M were determined through preliminary calculations of impact tests of the pump by hammer. Four impact tests were performed, where the knocking/measuring points are P_3/P_1, P_{15}/P_{15}, P_{19}/P_{19}, and P_{21}/P_{21}, respectively (see Fig. 9). The processes were simulated with different kinds of fixing boundaries. By comparing simulated vibration spectra with measured data, we determined a boundary condition such that the nozzles, feet, and knock-pin were completely fixed. Fig. 8 shows a spectrum of the calculated vibrations at this boundary in comparison with the measured ones, where the knocking/measuring places are P_3/P_1.

5. Results and discussions

5.1. Quantitative estimations to the vibration

The simulation results were compared with the measured data with respect to 23 points on the outer surface of the pump, whose positions are illustrated in Fig. 9. Points 1–8 are distributed equally on the periphery of a radial section in the inlet side body (cutting the second diffuser), points 9–15 are on a radial section in the outlet side body (cutting the fourth diffuser), and points 16–23 are located at sections of the inlet and outlet nozzles. Fig. 10 illustrates a typical power spectrum of the vibration velocity that was sampled at point 3 (located in the inlet body). The spectrum was obtained by a Fourier transform that is formulated in the Appendix. The vibration velocity was normalized by the impeller tip velocity, i.e.

$$V = v/v_{\text{tip}}, \tag{14}$$

where v is the velocity in the surface normal direction. This is in the spectrum where structural vibration is dominated by the BPF components. Because the BPF vibrations arise from rotor–stator interactions, the results validated the assumptions of Section 2. However, the average level of trivial vibrations is slightly lower in the experiment. This minor discrepancy may be because of high-level environmental noise at the experiment site or the setting of the viscosity c_M in the structural simulation. Another reason may be methodological, in that in the coupled simulation only the dynamic surface pressure is used—the noise contributions of the monopole and quadrupole fluid-acoustic sources are neglected. As these low-level noises are not the object of noise control, this discussion focuses on the BPF components.

Fig. 11 shows the BPF amplitudes of ωZ_i at points 1–5, and the overall values of ωZ_i at points 1–7. Table 1 lists the average and maximum error between the overall values of the simulation and the experiment at the body and nozzle measure points. The errors were estimated by the following equation:

$$(\delta v)_{OA} = \sum_{i=1}^{7} (v_{\text{FEM}} - v_{\text{EXP}})_{i\omega Z_i} \times 100\% \Big/ \sum_{i=1}^{7} (v_{\text{EXP}})_{i\omega Z_i}, \tag{15}$$

where the subscripts FEM and EXP represent the results of FEM simulation and those of the experiment, respectively. In a global view, the numerical results of 1-, 2-, 3-, and $5\omega Z_i$ agree with the measured values reasonably well. However, large discrepancies exist in the results of $4\omega Z_i$. The predicted amplitude of $4\omega Z_i$ is quite high, whereas the experiment indicates it is very low. The discrepancies will be discussed in detail in Section 5.3. Concerning the spatial distribution of the error, the vibration evaluation for the pump's body is better than that for the nozzles. The average error is 32% for the body and 76% for the nozzles. The relatively large error at the nozzles is caused by the mesh quality there. Although most of the pump has sufficiently fine elements, in the narrow areas of the nozzle there is only one grid layer. Because of the relatively coarse mesh in the nozzle portions, vibration characteristics there tend to be stiff.

5.2. Origination and spatial distribution of the BPF noise

The vibration modes and velocity distributions of the BPF components were extracted and visualized by Fourier transform for the vibration velocities of all mesh nodes. Although this paper cannot show animations, the velocity distribution at the outer surface plotted in Fig. 12 does provide straightforward information concerning the noise sources. This figure shows that among the first five basic BPFs, the vibrations of 2- and $5\omega Z_i$ represent the two main noise sources. The vibration of $2\omega Z_i$ mainly exists in the middle body and the two nozzles, while that of $5\omega Z_i$ seems to

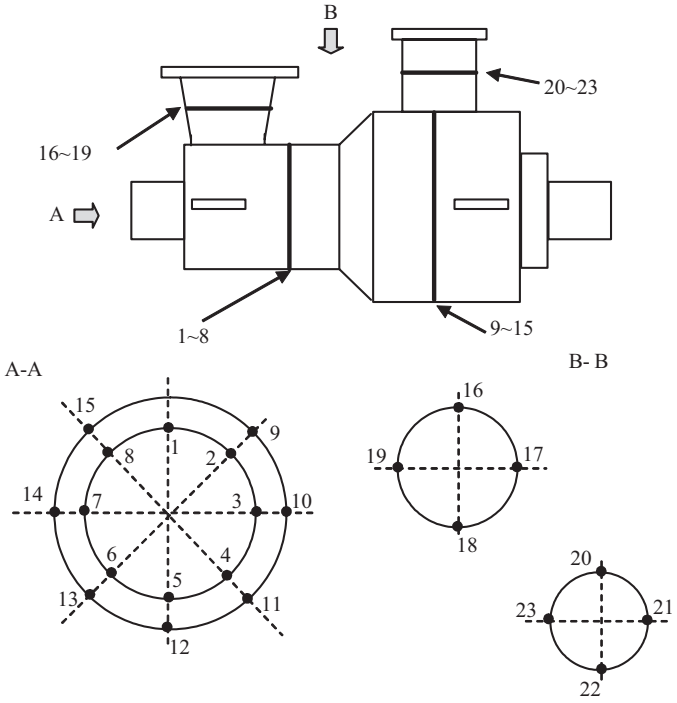

Fig. 9. Positions of the measuring and data sampling point set on the pump's outer surface.

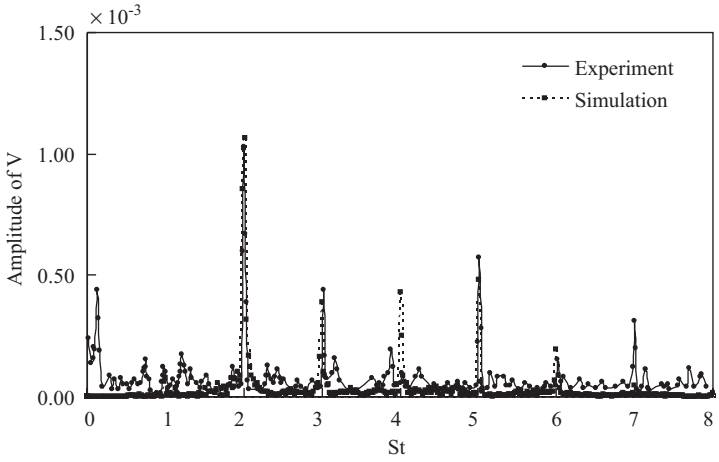

Fig. 10. Measured and calculated power spectra of vibration velocity at P_3.

be evenly distributed in the body. Visualizing the vibration modes, the propagation process, and the spatial distribution provides information about where the noises originate and what measures to take to reduce them.

5.3. Discussion on simulation accuracy

Although the vibration estimation is reasonably accurate, there exist some localized discrepancies, such as the large difference between predicted and actual vibrations of $4\omega Z_i$ and the error at the two nozzles. In fact, Fig. 12(d) shows that the large erroneous vibrations calculated for $4\omega Z_i$ are located at the underside of the two nozzles. This might come

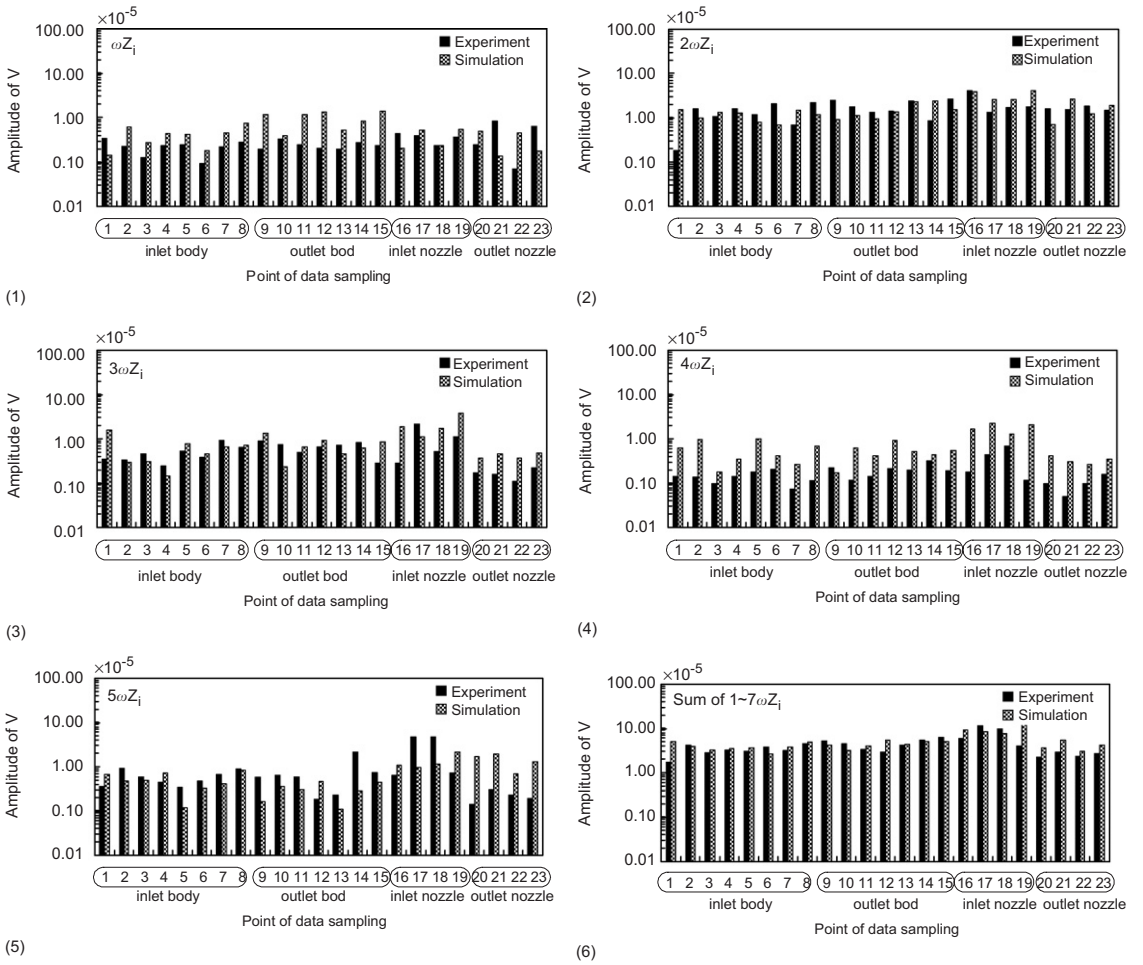

Fig. 11. Comparisons of the BPF vibration velocities at the sampling points (normalized by impeller tip speed). (1) ωZ_i, (2) $2\omega Z_i$, (3) $3\omega Z_i$, (4) $4\omega Z_i$, (5) $5\omega Z_i$ and (6) sum of $1–7\omega Z_i$.

Table 1
Relative errors of the predicted overall vibration velocities of 1 to $7\omega Z_i$ (%)

	Body (1–15)	Nozzles (16–23)	Whole surface (1–23)
Average	32	76	36
Maximum	52	136	136

from removing the connecting pipelines. In the experiment, the pipe vibrates with the pump's body, which allows its inertia to damp the vibrations a great deal; however, in the simulation the nozzle flanges are fixed. The simulation does not consider additional damping. In future studies, the results could be improved by several means: (i) set the boundary conditions of the two nozzles more accurately by adding pipeline meshes or a reliable model for the pipe's damping property and stiffness. (ii) Reduce the error in the nozzles by refining the grid or by applying a high-order discretization scheme. (iii) In the simulation, the damping viscosity of the pump was determined by impact tests with a hammer; however, this did not include the damping of the added fluid mass. This could account for the local discrepancies. This can be resolved by introducing a fluid–structure damping model or by developing a coupled analysis through the integration of fluid-acoustic simulation with structural simulation. (iv) There is a problem in modelling the connections

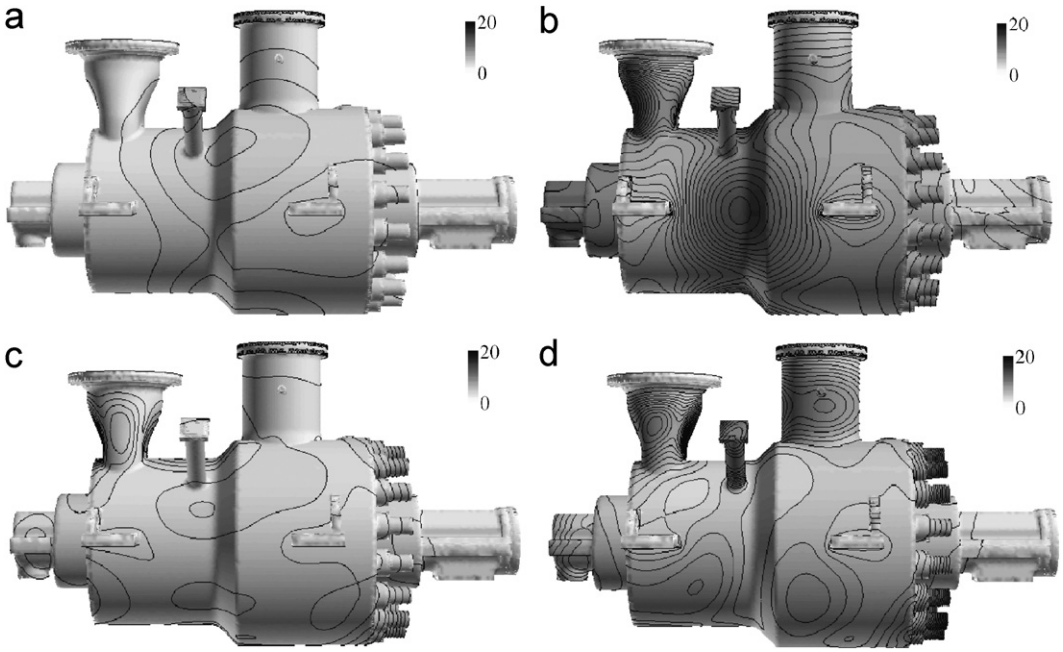

Fig. 12. Contours of the BPF vibration velocities on the pump's outer surface (normalized by impeller tip speed, $\times 10^{-5}$). (a) ωZ_i, (b) $2\omega Z_i$, (c) $3\omega Z_i$, and (d) $4\omega Z_i$.

between the inner and outer pump casing. In reality, the double-layered casing has damping connections at the connections. In our simulation, the mesh model treated the double layers as one, making its inherent vibrations different from reality. A contact simulation for this double-layered structure would provide a more accurate simulation.

6. Conclusions

This study developed a full-scale fluid–structural–acoustic numerical algorithm for quantitative estimation of the fluid-induced noise in turbomachinery. The structural simulation is coupled with the hydrodynamic flow field (calculated by LES simulation) through a data interface. The following results were obtained, demonstrating the feasibility of the algorithm:

(i) For BPF vibrations, qualitatively, the simulation results agree well with the experimental measurements. Some minor errors call for improvements with respect to the modelling and numerical methods.
(ii) The BPF vibrations were extracted and visualized by Fourier transform. From inner to outer surface, the propagation, modes, and spatial distribution of the vibrations were illustrated for the first time, providing guidelines for noise-reduction measures.

The computations provided the vibration velocities of the outer surface nodes. Takano et al. (2005) used this data to perform acoustic simulation using SYSNOISE to calculate noise emissions to the environment. The simulation results agreed with measured noise levels.

Acknowledgments

This work is funded by the program 'Frontier Simulation Software for Industrial Science (FSIS), 2002–2005' organized by the Ministry of Education, Culture, Sport, Science, and Technology of Japan (http://www.fsis.iis.u-tokyo.ac.jp/).

Appendix A. Spectral analysis by Fourier transform

For a time series of M samples, $S_k = S_k(k\tau)$, $k = 1, 2, \ldots, M$, with a time increment of τ, the period is $T = M\tau$. By Fourier transforms, we have

$$X_m = \frac{1}{M}\sum_{k=0}^{M-1} S_k e^{-2\pi\sqrt{-1}km/M}, \quad S_k = \sum_{m=0}^{M-1} X_m e^{2\pi\sqrt{-1}km/M}, \tag{A.1}$$

where X_m is the complex coefficient at frequency m/T, and the real and imaginary parts are $\Re(X_m)$ and $\Im(X_m)$, such that

$$X_m = \Re(X_m) + i\Im(X_m), \tag{A.2}$$

$$\Re(X_m) = \frac{1}{M}\sum_{k=0}^{M-1} S_k \cos(2\pi km/M), \tag{A.3}$$

$$\Im(X_m) = -\frac{1}{M}\sum_{k=0}^{M-1} S_k \sin(2\pi km/M). \tag{A.4}$$

The amplitude P_m of vibration at frequency m/T is

$$P_m = \sqrt{2}|X_m| = \sqrt{2}[\Re(X_m)^2 + \Im(X_m)^2]^{1/2}. \tag{A.5}$$

The computational effort for the Fourier transform of a whole spectrum is proportional to $M \log M$. In the case of the Fourier transform for all the mesh nodes, only the amplitudes of the BPF vibrations were calculated. This saves calculation time. If the total number of samples M is specified in advance, the Fourier transform can be done during the simulation, requiring no time series data.

References

Chu, S., Dong, R., Katz, J., 1995. Relationship between unsteady flow, pressure fluctuations, and noise in a centrifugal pump—Parts A and B. ASME Journal of Fluids Engineering 117, 24–35.

Dong, R., Chu, S., Katz, J., 1997. Effect of modification to tongue and impeller geometry on unsteady flow, pressure fluctuations, and noise in a centrifugal pump. ASME Journal of Turbomachinery 119, 506–515.

Ffowcs Williams, J.E., Hawkings, D.L., 1969. Sound generation by turbulence and surfaces in arbitrary motion. Philosophical Transactions of the Royal Society (London) A 264, 321–342.

Guelich, J.F., Bolleter, U., 1992. Pressure pulsations in centrifugal pumps. ASME Journal of Vibration and Acoustics 114, 272–279.

Howe, M.S., 1991. On the estimation of sound produced by complex fluid–structure interactions, with application to a vortex interacting with a shrouded rotor. Proceedings of the Royal Society (London) A 433, 573–598.

Kato, C., Kaiho, M., Manabe, A., 2003. An overset finite-element Large-Eddy Simulation method with applications to turbomachinery and aeroacoustics. Journal of Applied Mechanics 70, 97–108.

Kato, C., Yoshimura, S., Yamade, Y., Jiang, Y.Y., Wang, H., Imai, R., Katsura, H., Yoshida, T., Takano, Y., 2005. Prediction of the noise from a multi-stage centrifugal pump. ASME-FED paper; FEDSM2005-77312.

Katsura, H., Yoshida, T., 2003, Measurements of fluid pressure fluctuation in a multi-stage centrifugal pump, HIC (Hitachi Industries Co.) Report, No. DD1-0-00GX-000003.

Langthjem, M.A., Olhoff, N., 2004a. A numerical study of flow-induced noise in a two-dimensional centrifugal pump. Part I. Hydrodynamics. Journal of Fluids and Structures 19, 349–368.

Langthjem, M.A., Olhoff, N., 2004b. A numerical study of flow-induced noise in a two-dimensional centrifugal pump Part II. Hydroacoustics. Journal of Fluids and Structures 19, 369–386.

Lighthill, M.J., 1952. On sound generated aerodynamically. I. General theory. Proceedings of the Royal Society (London) A 211, 564–587.

Mongeau, L., Thompson, D.E., McLaughlin, D.K., 1995. A method for characterizing aerodynamic sound sources in turbomachines. Journal of Sound and Vibration 181, 369–389.

Morgenroth, M., Weaver, D.S., 1996. Sound generation by a centrifugal pump at blade passage frequency. In: Proceedings of Flow-Induced Vibrations 1996, Montreal, pp. 455–463.

Rzentkowski, G., 1996. Generation and control of pressure pulsations emitted from centrifugal pumps: a review. In: Proceedings of Flow-Induced Vibrations 1996, Montreal, pp. 439–454.

Rzentkowski, G., Zbroja, S., 2000. Experimental characterization of centrifugal pumps as an acoustic source at the blade-passing frequency. Journal of Fluids and Structures 14, 529–558.

Sekita, D., Okuda, H., Yagawa, G., 2001. A general loosely coupling tool for parallel FEM programs. Transactions of JSCES 3, 207–212 (in Japanese).

Takano, Y., Jiang, Y.Y., Yoshimura, S., Imai, R., Nemoto, K., Katsura, H., Yoshida, T., Kato, C., 2005. Numerical simulation of radiation noise from a full-scale multi-stage centrifugal pump. In: 12th International Congress on Sound and Vibration, No. 731, Lisbon, Portugal.

Wang, H., Kato, C., Yamade, Y., Katsura, H., Yoshida, T., 2004. Large Eddy Simulation of unsteady flow in a centrifugal pump. In: Proceedings of the Third International Symposium on Fluid Machinery and Fluid Engineering, Beijing, China, pp. 168–173.